Title

Virtual Impactor-Based Label-Free Pollen Detection using Holography and Deep Learning

Journal

ACS Sensors, 7(12)

ISSN

2379-3694

Authors

Luo, Yi

Zhang, Yijie

Liu, Tairan

et al.

Publication Date

2022-12-23

DOI

10.1021/acssensors.2c01890

Virtual impactor-based label-free pollen detection using holography and deep learning

Yi Luo[1,2,3,+], Yijie Zhang[1,2,3,+], Tairan Liu[1,2,3], Alan Yu[1,4], Yichen Wu[1,2,3] and Aydogan Ozcan[1,2,3]*

[1]Electrical and Computer Engineering Department, University of California, Los Angeles, California 90095, USA

[2]Bioengineering Department, University of California, Los Angeles, California 90095, USA

[3]California Nano Systems Institute (CNSI), University of California, Los Angeles, California 90095, USA

[4]Computer Science Department, University of California, Los Angeles, California 90095, USA

[+]Equal contributing authors

[*]Correspondence: Prof. Aydogan Ozcan

E-mail: ozcan@ucla.edu

Address: 420 Westwood Plaza, Engr. IV 68-119, UCLA, Los Angeles, CA 90095, USA

Tel: +1(310)825-0915

Fax: +1(310)206-4685

Abstract

Exposure to bio-aerosols such as pollen can lead to adverse health effects. There is a need for a portable and cost-effective device for long-term monitoring and quantification of various types of pollen. To address this need, we present a mobile and cost-effective label-free sensor that takes holographic images of flowing particulate matter concentrated by a virtual impactor, which selectively slows down and guides particles larger than 6μm to fly through an imaging window. The flowing particles are illuminated by a pulsed laser diode, casting their inline holograms on a CMOS image sensor in a lens-free mobile imaging device. The illumination contains three short pulses with a negligible shift of the flowing particle within one pulse, and triplicate holograms of the same particle are recorded at a single frame before it exits the imaging field-of-view, revealing different perspectives of each particle. The particles within the virtual impactor are localized through a differential detection scheme, and a deep neural network classifies the pollen type in a label-free manner, based on the acquired holographic images. We demonstrated the success of this mobile pollen detector with a virtual impactor using different types of pollen (i.e., bermuda, elm, oak, pine, sycamore, and wheat) and achieved a blind classification accuracy of 92.91%. This mobile and cost-effective device weighs ~700 g and can be used for label-free sensing and quantification of various bio-aerosols over extended periods since it is based on a cartridge-free virtual impactor that does not capture or immobilize particulate matter.

Keywords

Deep learning-based sensing, label-free sensing, air quality measurement, pollen detection using virtual impactors, digital holography

Bio-aerosols account for 5-34% of indoor particulate matter (PM)[1]. They are airborne microparticles originating from plants, animals, and living or dead microorganisms[2]. Bio-aerosols can easily enter the respiratory tract during inhalation due to their microscopic size. Exposure to bio-aerosols has been related to a wide range of health issues[3,4]. Some bio-aerosols cause irritation and allergic reactions, such as pollen[5,6]; some others, like fungal and bacterial[7,8] PM, can spread infectious and respiratory diseases. For example, bio-aerosols served as an important transmission route during the COVID-19 pandemic[9,10]. They may also lead to an increased risk of cancer[4,11,12]. Conventional sensing of bio-aerosols includes two steps: the aerosols are first sampled using, e.g., an impinger, a cyclone, an impactor, or a filter[13,14], and then analyzed in a central lab under a microscope with fluorescence labeling or through a culture-based procedure by a microbiology expert[15]. Other technologies, such as polymerase chain reaction (PCR)[16] and enzyme-linked immunosorbent assays (ELISA)[17], are also applied to better identify the captured bio-aerosols with high sensitivity and specificity. However, the complicated procedures and the need for well-trained experts hinder their widespread use for continuous monitoring of human exposure to bio-aerosols.

For field-portable bio-aerosol monitoring devices that integrate aerosol sampling and inspection, a major challenge is identifying the collected particles. Most devices avoid this challenge by selectively sampling a few types of bio-aerosols using specific antibodies. This antibody-antigen specific reaction can be sensed using different mechanisms, such as lateral flow-based immunoassays[18], vibrational cantilevers[19], surface plasmon resonance-based sensors[20], or Raman spectroscopy[21]. However, the immunoreaction limits the throughput of the device and the amount of aerosols that can be immobilized, and non-specific binding events can cause false-positive detections. Also, the utilization of antibodies creates storage and shelf-life-time issues for these sensors, and it lacks scalability to cover a larger variety of bio-aerosols that might be present in different parts of the world during different seasons. In another embodiment, analyzing the autofluorescence signals of individual bio-aerosols excited by ultraviolet (UV) light was utilized as a label-free method for bio-aerosol detection[22,23], but this approach suffered from low specificity due to the insufficient information provided by the weak autofluorescence signals. As an alternative approach, a field-portable, cost-effective platform for high-throughput quantification of aerosols using mobile microscopy was also reported[24,25]. This device incorporates an impaction-based aerosol sampling method: a high-speed airstream carries particles moving from the impactor nozzle

to a transparent polymer substrate that faces the inlet flow direction. Large aerosols detach from the streamline due to their inertia and are physically collected/captured by the substrate. However, the transparent impactor used for particle collection in this platform suffers from an overfill of the sampling substrate: excessive particles captured on the polymer substrate occlude the imaging field-of-view, preventing new particles from being detected. Therefore, the impactor cartridge must be frequently replaced, which makes the platform inadequate for long-term unsupervised operation.

A good substitution for a physical impactor can be a virtual impactor, which replaces the collection substrate of an impactor with a middle channel (a collection probe)[26], where only a minor portion of the input flow will go through. Most of the input air leaves the device via by-pass channels, leading to a sharp flow direction change, where large particles detach from the major streamline and enter the middle channel, as their greater inertia prevents them from following the drastic flow direction change. Consequently, particles are separated based on their inertia, and large ones are concentrated inside the middle channel. Virtual impactors have been widely implemented for ambient fine particle sensing[27–29], especially monitoring PM in air[30–35]. Recent efforts have also utilized this platform for bio-aerosol detection in indoor environments[36,37]. However, to classify the type of the collected particles for bio-aerosol sensing, the airflow from the middle channel needs to go through a filtration step, where the flowing bio-aerosols are transferred to a physical filter[37] or a bio-aerosol collector (an impinger)[38]. Further analytical examination steps, such as culturing and PCR analysis[39], are applied to reveal the species of the collected bio-aerosols.

In this work, we present a virtual impactor-based, cartridge- or filter-free pollen detection method that combines computational imaging and deep learning to sense and classify pollen particles without any external labels or chemical sample processing steps (Fig. 1(a)). Different types of pollen (including bermuda, elm, oak, pine, sycamore and wheat) were selected as representative bio-aerosols because of their wide-spread existence and potential allergenic hazard. For instance, just the oak pollen makes up ~20% of allergic pollen in North America[40] and exposure to oak pollen may induce respiratory symptoms such as allergic rhino-conjunctivitis[41,42], allergic rhinitis[43,44], and asthma[45] in sensitive individuals. In our mobile and cost-effective device, a virtual impactor was designed and 3D printed to concentrate the flowing particles larger than ~6 μm, which covers the size range of most pollen species. An imaging window with a sensing volume of 25 mm^3 was placed on the middle channel, and inline lensfree holography was used to image the passing-by particles,

owing to its capability of recording volumetric information with a large field-of-view[46–52]. Coherent illumination from a laser diode shined through the imaging window, forming inline holograms on a complementary metal-oxide semiconductor (CMOS) image sensor placed on the other side, right next to the imaging window (Fig. 1(b) and (c)). Three illumination pulses were fired during each frame, casting three different holographic images of each particle – all captured at the same frame. With each illumination pulse, a clear lensfree hologram of the particle that is free from motion blur and rolling shutter artifacts was captured by the CMOS image sensor. After three pulses, the CMOS image sensor integrated all three holograms of the same particle at three different lateral locations, forming a unique triplicate holographic pattern per flowing particle (Fig. 1(d)). The particles are localized by a differential detection algorithm, and a trained deep neural network was used to classify the pollen type of each particle from its auto-focused holograms. As a demonstration of the proof of concept of this mobile and cost-effective system, we imaged aerosols of six different types of pollen: bermuda, elm, oak, pine, sycamore and wheat, which are widespread in North America and Europe[53,54]. With the triplicate holographic patterns per particle, a majority voting was applied to the classification decision of each particle, achieving a pollen classification accuracy of 92.91% (Fig. 1(e)).

To the best of our knowledge, this is the first demonstration of an imaging-based virtual impactor design that enables label-free pollen detection using neural networks, without the need for any filtration or chemical processing. This device is compact, cost-effective and light-weight (~700 g) and since it does not require a cartridge or filter for pollen sensing, it enables air quality monitoring over an extended period of time without any supervision. This AI-based bio-aerosol detection and classification device provides a unique solution to indoor air quality monitoring and label-free bio-aerosol sensing.

Results

Portable pollen sampling device using a virtual impactor

Our portable device designed to sample and image pollen particles contains three major parts: a virtual impactor that collects and slows down the flowing pollens in its middle channel, a lens-free holographic imaging system capturing microscopic images of pollens, and a controlling circuit

automating the entire workflow. The virtual impactor contains one middle channel with a designed flow rate of 10 mL/min, and two symmetrical by-pass channels with a total flow rate of 1L/min. The physical dimensions of the virtual impactor were optimized by finite element method (FEM) simulations using COMSOL (Figs. 2(a) and (b)). Input aerosols larger than 6.3 μm aerodynamic diameter (see the Methods section for details) have more than 50% probability of entering the virtual impactor through the middle channel, while other smaller particles leave via by-pass channels (Fig. 2(c)). Based on this, the pollen particles to be detected and classified are concentrated in the middle channel, where the flow rate is ~100 times smaller than the input flow rate. Consequently, each pollen type of interest has a significantly higher concentration inside the middle channel than in ambient air. Two fans are used to power the flow inside the middle and by-pass channels independently, whose flow rates are monitored by two separate flow meters. The real-time signals are sent to an Arduino microcontroller, where a simple PID feedback loop was implemented to adjust the fans' speed (see Fig. 2(d) and Supplementary Fig. S1).

An imaging window with a volume of 5×5×1 mm^3 is opened at the center of the middle channel (Fig. 2(b)), sealed by coverslip glasses. A CMOS image sensor to capture the lensfree holograms of the particles flowing over the imaging window was placed next to the channel, touching the coverslip glass. The axial distance from the bottom of the channel to the CMOS sensor is ~1.5 mm. A customized Graphical User Interface (GUI) was designed to control the CMOS imager and take holographic videos at a frame rate of 3.5 fps. If CW illumination were to be used to form holograms, the high speed of the concentrated particles (~0.17m/s) would normally introduce a strong motion blur and rolling shutter artifacts. To capture motion blur-free and undistorted holograms, the imaging system was configured to mimic strobe photography (Fig. 1(d)). When all the pixels of the CMOS are turned on to collect photons, a signal was sent to our customized pulse generation circuit, firing a train of three successive pulses using a laser diode (λ=515nm) that shines through the imaging window. Under each laser pulse, all the flowing particles above the imaging window form their holograms captured by the CMOS image sensor. The pulse duration was short enough (6.9 μs) to avoid motion blur for each holographic pattern. The particles travel along the flow direction during the interval between two pulses ($\delta t = 699\mu s$). As a result, after the pulse train, three individual holograms were acquired by the CMOS image sensor, through a *single frame* with triplicate holographic patterns for each pollen particle flowing inside the middle channel. Each captured

hologram was transferred into the controlling laptop for further processing. The entire mobile device has dimensions of 24.1 cm×10.5 cm×10.2 cm and weighs ~700g. The components of our prototype cost ~$923 to build, and its detailed list can be found in Supplementary Table S1.

Label-free pollen imaging and classification

To demonstrate the proof-of-concept of our mobile device for label-free pollen detection, we targeted aerosols containing six different types of pollens: bermuda, elm, oak, pine, sycamore, and wheat. Purified aerosols containing only a single pollen type were generated using a customized particle generator that directly connects to our device (see Supplementary Figs. S2 and S3). In each measurement, the CMOS image sensor was configured to take 60 frames of time-lapse holographic images. Fifty different measurements were conducted on each type of pollen within a period of a month, without any need to replace the virtual impactor. This capability to conduct long-time experiments is a unique feature enabled by the virtual impactor, which does not immobilize the particles or create contamination on the imaging window.

These time-lapse holographic images monitor the particles passing through the imaging window above the image sensor. A flying particulate matter can be easily identified from the time-lapse holograms captured by the portable device (Fig. 3); without loss of generality, the triplicate holographic patterns of a flowing particle of interest appear in the second frame of any consecutive three-frame holograms: $H(t_0)$, $H(t_0+\Delta t)$ and $H(t_0+2\Delta t)$. A differential hologram H_d can be calculated from these three successive CMOS frames (Fig. 3), i.e.,

$$H_d = 2H(t_0+\Delta t) - \big(H(t_0+2\Delta t) + H(t_0)\big). \quad (1)$$

Note that Δt=285.7 ms and should not be confused with the interval between two successive pulses ($\delta t = 699\mu s$); the latter creates multiple holograms of each flowing particle on a single lensfree image frame, whereas Δt is determined by the frame rate of the CMOS imager (3.5 fps) . After this differential calculation, the flying particles of interest that only appear in the frame $H(t_0+\Delta t)$ present a lower intensity level compared to the background. A threshold was applied to H_d for localizing each flowing particle, and the resulting image patches with the detected particles were cropped, each with a size of 256×256 pixels.

The microscopic image of the flowing pollen in each region of interest (ROI) was reconstructed

by digitally propagating the raw hologram using the angular spectrum method to its focal plane, estimated by an autofocusing algorithm[55]. For all the six pollen species used in this work, the raw triplicate holograms of some representative particles and their back-propagated images are illustrated in Fig. 4. The back-propagated holograms of each pollen, without any motion blur or rolling shutter artifact, showed a good reconstruction fidelity. Importantly, the three holographic replicas of the same particle were not identical, which indicates that the particles have free rotation while flowing within the air stream. These images of each pollen from different perspectives provided richer information about the pollen, which proved important for more accurate classification of their type, as will be reported next.

An image dataset was established from the experimental data captured using our device, containing ~6000 ROIs for training and validation, and ~900 ROIs for blind testing. A deep neural network based on DenseNet201[56] was trained to classify the type of pollen particles. During the training, the network treated each ROI as an *independent* particle. In other words, the relation between the holographic replicas of each flowing particle was intentionally ignored to increase the robustness of our classification system. To utilize the volumetric information provided by lensfree holographic imaging, the network was trained with both the real and imaginary channels of each ROI propagated to five axial locations: its focus plane and 50μm and 100μm above and below the focus plane. After the training phase, the deep neural network achieved a blind testing accuracy of 90.48% in classifying all the individual ROIs containing 6 different types of pollen. The corresponding confusion matrix is displayed in Fig. 5(a). Using the additional information (with different perspectives of the pollen) available in triplicate holographic images of each flowing particle helps improve the final classification accuracy. The ROIs belonging to the same particle were first located and grouped together. To utilize this additional source of information, we devised a majority voting scheme applied to the labels of the three successive ROIs (corresponding to three holographic replicas of the same particle), which were independently classified using the same trained network. The voting winner (with 2 or more votes) was selected as the final predicted label (pollen type) for all three replicas of each flowing pollen particle, which increased the blind testing accuracy to 92.91% (see the confusion matrix in Fig. 5(b)).

Discussion

The presented particle classification scheme using triplicate holographic images has a unique advantage since it permits the visualization of the same particle from different perspectives during its flow within the virtual impactor. The impact of this capability can be better seen in the classification of pine pollens. In general, pine pollens have a unique feature with wing-like bladders (see the fourth column in Fig. 4 as an example). During its flow inside the virtual impactor channel, there is a chance that the captured hologram of a pine pollen only reflects its main body, with the bladders hidden behind it, which makes it resemble a wheat pollen of similar size (see Supplementary Fig. S4 as an example). In fact, because of this, the trained neural network misclassified 22.97% of pine pollens as wheat using a single holographic image. The classification accuracy of pine pollens was improved using the triplicate holographic images through a majority voting process, reducing the error rate to 18.57%. Furthermore, if we relax our voting rule for pine pollens such that all the particles in triplicate holographic images will be labeled as pine pollens if at least one of those holographic images was classified as pine, the error rate can further drop to 17.14%. From the perspective of allergies, this remaining mislabeling of pine pollen (~17%) as wheat would not necessarily mislead the potential users since many people that are sensitive to pine pollen are also allergic to other pollen[57].

The designed virtual impactor device with lens-free holographic imaging also presents a unique feature of volumetric sensing of flowing particulate matter. It allows us to image flowing particles distributed inside a large volume (25 mm^3) and records the 3D information about the particles through holography. Harvesting this 3D information, in this work, we demonstrated a deep neural network that utilizes the complex-valued images of each flowing particle at five different axial locations, each of which has different phase and amplitude profiles, reflecting the unique 3D refractive index information of the particle. To shed more light on the classification advantages brought by this volumetric sensing approach, we further trained another deep neural network taking only the auto-focused images, i.e., from a single axial location, while keeping the architecture and training parameters the same as before. This network that only used the complex-valued object field from a single axial plane achieved a worse classification accuracy of 85.23%, which indicates the advantages of using multiple complex fields at different axial planes for each flowing particle.

Generally, the quality of an inline holographic image after a simple auto-focusing step suffers from the twin-image artifact unless phase recovery is applied to it. In this study, however, since the distance between the samples and the CMOS image sensor is relatively large (on average ~ 2 mm), we did not use phase retrieval and the twin image artifact did not constitute an obstacle to the accurate classification of pollen particles. In case a more clear microscopic image of each flowing particle is desired, iterative or neural network-based phase recovery algorithms[58–61] can be used to remove the twin-image artifacts, revealing increased contrast and SNR for each particle. In addition, deep neural networks can also be used for auto-focusing and phase recovery at the same time[60,62,63]. The inclusion of these additional processing steps might further improve the performance of our virtual impactor-based label-free bio-aerosol detection and classification device.

In our proof-of-concept demonstration reported in this work, the image processing was done offline on a computer. However, this does not limit our sensing throughput. The CMOS image sensor is controlled by a C++ program, which can be transferred to other portable platforms. Our differential imaging-based particle/pollen detection algorithm can be easily handled by a light-weight device. Each cropped particle FOV can be either processed on the cloud[24] or on-the-spot, and the neural network-based processing can be covered by edge computing units such as Nvidia Jetson One[64].

While this work utilized a virtual impactor device to sample and concentrate pollen particles in air, it is also conceivable that, with various advances made in the microfluidics field, different sampling methods can also be used to separate particles/pollen based on their size or inertia[65–67], especially if the pollens are pre-sampled through an aqueous solution[68]. The pulsed illumination system adopted in our device is also suitable for high fidelity imaging of flowing particles within microfluidic channels if an alternative, fluidic-based pollen collection method were to be implemented.

Conclusion

In conclusion, we presented a novel device for label-free pollen detection using a virtual impactor and computational imaging. Pollen particles in the air were slowed down and concentrated

in the middle channel of a virtual impactor. Pulsed illumination was used to form triplicate holographic patterns of the same particle on a single frame. The volumetric sensing provided by holographic multi-shot imaging of the same flowing particle brought unique features to this device, using which a deep neural network achieved 92.91% accuracy in classifying different types of pollens. The mobile device prototype costs ~$920 and weighs ~700g, which can be further reduced in mass production, providing a cost-effective and portable solution to long-term unattended personalized bio-aerosol monitoring.

Methods

Virtual impactor design and fabrication

The virtual impactor separates aerosols based on their aerodynamic diameter d_a. For an arbitrary particle, d_a can be calculated as

$$d_a = d_e \left(\frac{\rho_p}{\rho_0 \chi}\right)^{\frac{1}{2}} \quad (2),$$

where d_e is the diameter of a spherical particle with the same volume, ρ_p and ρ_0 refer to the density of the particle and water, respectively. χ is the dynamic shape factor calculated based on the microscopic shape of the particle[26]. The cut-off diameter (d_{50}) of a virtual impactor is the aerodynamic diameter of a particle that has 50% probability to be collected by the middle channel, resulting in a particle collection efficiency of 50%. It can be estimated using the flow velocity and the virtual impactor geometry[26]:

$$d_{50} = \sqrt{\frac{9\eta W^2 L(Stk_{50})}{\rho_p Q}} - 0.0078 \times 10^{-6} \quad (3)$$

where η is the air viscosity. W and L denote the width and length of the impaction nozzle (the junction of the middle and by-pass channels). In this work, we used W=5 mm and L=1 mm (see Supplementary Fig. S5 for details). Stk_{50} is the Stokes number of the particles with 50% collection efficiency, ρ_p is the density of the particle, and Q is the flow rate. In designing the virtual impactor, the flow rate Q was first empirically chosen, and the dimension of the virtual impactor nozzle was optimized using the FEM solver in COMSOL (see Fig. 2(a)). The virtual impactor channel was fabricated using a 3D printer (Objet30 Pro, Stratasys Inc.) with a light-blocking material. The region

designed for the imaging window was fabricated as open holes during the 3D printing. Coverslip glasses were used to seal them and form an air-tight channel.

Camera exposure settings and illumination pulse synchronization

The CMOS sensor (IDS-UI-3592LE-C-VU, 4912 x 3684 pixels, pixel pitch 1.25μm) used in this work operates based on a rolling shutter with a global release feature. The camera sequentially turns on all 4912 rows of pixels to start collecting photons, from top to bottom, and sequentially turns them off. The time between the bottom row of the pixels to start detecting photons and the top row to stop detecting photons was set to be 2600 μs. In other words, all pixels on the CMOS sensor collect photons during this 2600 μs period. A high voltage level is provided when all pixels are turned on. This signal triggers a single pulse with a duration of 1600 μs from a re-triggerable monostable multivibrator (74LS123, Texas Instrument Inc.). This single pulse is further coupled with a pulse train generated by a 555 timer (LMC555CN, Texas Instrument Inc.) with a pulse width of 6.9 μs and a period of 707 μs. Three pulses (each having 6.9 μs) are generated and sent to an LED controller (TLC5917, Texas Instrument Inc.), which injects 120 mA current into the laser diode (PLT5 510, OSRAM Opto Semiconductors GmbH).

Neural network training

The network used in this work was adapted from DenseNet201[56], with the channel number of the first convolutional layer tuned to match the input image channels. In the network training, each ROI was first randomly cropped to have a size of 224×224 pixels. Data augmentation, including random flipping and rotation, was consequently applied to the images. Finally, before being fed into the networks, each input image was processed with a Gaussian blur to remove salt and pepper noise caused by the short exposure under each pulsed illumination (6.9 μs). A softmax cross entropy loss was calculated using the network predicted class scores and the ground truth pollen species as:

$$\mathcal{L}_I = -\sum_{c=1}^{6} g_c \cdot \log\left(\frac{\exp(s_c)}{\sum_{c'=1}^{6}\exp(s_{c'})}\right) \quad (4),$$

where s_c denotes the predicted class score for the c^{th} class, and g_c denotes the c^{th} entry of the ground truth label vector. The network parameters were optimized using an Adam optimizer, with

the learning rate set to be 1×10^{-4} at the beginning and tuned using a cosine annealing schedule. The network was trained using a desktop computer with a Ryzen 9 3950X central processing unit (AMD Inc.) and an RTX 2080Ti graphic processing unit (GPU, NVidia Inc.) with 64 GB of memory, running on Windows 10 (Microsoft Inc.). The typical training time with 200 epochs is ~5 hours.

Acknowledgement

The authors acknowledge Derek Tseng of UCLA for his help in 3D printing.

Author contributions

Y.L. and Y.Z. performed the design of the systems and conducted the experiments. T.L. and A.Y. provided assistance with the design of the system. All the authors participated in the analysis and discussion of the results. Y.L., Y.Z. and A.O. wrote the manuscript with assistance from all the authors. A.O. conceived and initiated the project and supervised the team.

Conflict of interests

The authors declare no conflict of interests.

Funding

Ozcan Lab at UCLA acknowledges the funding of Koç Group and the Tobacco-Related Disease Research Program.

Supporting Information

Supplementary Table S1: Purchase costs of the components used in our mobile pollen sensor prototype.
Supplementary Figures S1-S5: Control circuit design. A photograph of the experimental setup. Customized particle generator design. Examples of pine pollen image fields-of-view and the deep neural network classification results. Schematic drawing of the virtual impactor nozzle.

Notes

The design files of our device can be found at:
https://github.com/Yijie-Zhang/Virtual-impactor-CAIR.

References

(1) Mandal, J.; Brandl, H. Bioaerosols in Indoor Environment - A Review with Special Reference to Residential and Occupational Locations. *The Open Environmental & Biological Monitoring Journal* **2011**, *4* (1).

(2) Douwes, J.; Eduard, W.; Thorne, P. S. Bioaerosols. In *International Encyclopedia of Public Health*; Heggenhougen, H. K. (Kris), Ed.; Academic Press: Oxford, 2008; pp 287–297. https://doi.org/10.1016/B978-012373960-5.00281-1.

(3) Douwes, J.; Thorne, P.; Pearce, N.; Heederik, D. Bioaerosol Health Effects and Exposure Assessment: Progress and Prospects. *Ann Occup Hyg* **2003**, *47* (3), 187–200. https://doi.org/10.1093/annhyg/meg032.

(4) Humbal, C.; Gautam, S.; Trivedi, U. A Review on Recent Progress in Observations, and Health Effects of Bioaerosols. *Environment International* **2018**, *118*, 189–193. https://doi.org/10.1016/j.envint.2018.05.053.

(5) D'Amato, G.; Cecchi, L.; Bonini, S.; Nunes, C.; Annesi-Maesano, I.; Behrendt, H.; Liccardi, G.; Popov, T.; Van Cauwenberge, P. Allergenic Pollen and Pollen Allergy in Europe. *Allergy* **2007**, *62* (9), 976–990. https://doi.org/10.1111/j.1398-9995.2007.01393.x.

(6) Idrose, N. S.; Lodge, C. J.; Erbas, B.; Douglass, J. A.; Bui, D. S.; Dharmage, S. C. A Review of the Respiratory Health Burden Attributable to Short-Term Exposure to Pollen. *International Journal of Environmental Research and Public Health* **2022**, *19* (12), 7541. https://doi.org/10.3390/ijerph19127541.

(7) Fung, F.; Hughson, W. G. Health Effects of Indoor Fungal Bioaerosol Exposure. *Applied Occupational and Environmental Hygiene* **2003**, *18* (7), 535–544. https://doi.org/10.1080/10473220301451.

(8) Green, C. F.; Scarpino, P. V.; Gibbs, S. G. Assessment and Modeling of Indoor Fungal and Bacterial Bioaerosol Concentrations. *Aerobiologia* **2003**, *19* (3/4), 159–169. https://doi.org/10.1023/B:AERO.0000006531.35387.bd.

(9) Anderson, E. L.; Turnham, P.; Griffin, J. R.; Clarke, C. C. Consideration of the Aerosol Transmission for COVID-19 and Public Health. *Risk Analysis* **2020**, *40* (5), 902–907. https://doi.org/10.1111/risa.13500.

(10) Tellier, R. COVID-19: The Case for Aerosol Transmission. *Interface Focus* **2022**, *12* (2), 20210072. https://doi.org/10.1098/rsfs.2021.0072.

(11) Kim, K.-H.; Kabir, E.; Jahan, S. A. Airborne Bioaerosols and Their Impact on Human Health. *Journal of Environmental Sciences* **2018**, *67*, 23–35. https://doi.org/10.1016/j.jes.2017.08.027.

(12) Lee, L. D.; Berkheiser, M.; Jiang, Y.; Hackett, B.; Hachem, R. Y.; Chemaly, R. F.; Raad, I. I. Risk of Bioaerosol Contamination With Aspergillus Species Before and After Cleaning in Rooms

Filtered With High-Efficiency Particulate Air Filters That House Patients With Hematologic Malignancy. *Infection Control & Hospital Epidemiology* **2007**, *28* (9), 1066–1070. https://doi.org/10.1086/519866.

(13) Ghosh, B.; Lal, H.; Srivastava, A. Review of Bioaerosols in Indoor Environment with Special Reference to Sampling, Analysis and Control Mechanisms. *Environment International* **2015**, *85*, 254–272. https://doi.org/10.1016/j.envint.2015.09.018.

(14) Haig, C. W.; Mackay, W. G.; Walker, J. T.; Williams, C. Bioaerosol Sampling: Sampling Mechanisms, Bioefficiency and Field Studies. *Journal of Hospital Infection* **2016**, *93* (3), 242–255. https://doi.org/10.1016/j.jhin.2016.03.017.

(15) Eduard, W. The Performance of Culture-Based Methods and Microscopy for Quantification of Noninfectious Airborne Microorganisms in Epidemiological Studies of Highly Contaminated Work Environments. *AIHA Journal* **2003**, *64* (5), 684–689. https://doi.org/10.1080/15428110308984864.

(16) DeAngelis, K. M.; Wu, C. H.; Beller, H. R.; Brodie, E. L.; Chakraborty, R.; DeSantis, T. Z.; Fortney, J. L.; Hazen, T. C.; Osman, S. R.; Singer, M. E.; Tom, L. M.; Andersen, G. L. PCR Amplification-Independent Methods for Detection of Microbial Communities by the High-Density Microarray PhyloChip. *Appl. Environ. Microbiol.* **2011**, *77* (18), 6313–6322. https://doi.org/10.1128/AEM.05262-11.

(17) Verma, J.; Saxena, S.; Babu, S. G. ELISA-Based Identification and Detection of Microbes. In *Analyzing Microbes: Manual of Molecular Biology Techniques*; Arora, D. K., Das, S., Sukumar, M., Eds.; Springer Protocols Handbooks; Springer Berlin Heidelberg: Berlin, Heidelberg, 2013; pp 169–186. https://doi.org/10.1007/978-3-642-34410-7_13.

(18) Lee, I.; Seok, Y.; Jung, H.; Yang, B.; Lee, J.; Kim, J.; Pyo, H.; Song, C.-S.; Choi, W.; Kim, M.-G.; Lee, J. Integrated Bioaerosol Sampling/Monitoring Platform: Field-Deployable and Rapid Detection of Airborne Viruses. *ACS Sens.* **2020**, *5* (12), 3915–3922. https://doi.org/10.1021/acssensors.0c01531.

(19) Johnson, B. N.; Mutharasan, R. Biosensing Using Dynamic-Mode Cantilever Sensors: A Review. *Biosensors and Bioelectronics* **2012**, *32* (1), 1–18. https://doi.org/10.1016/j.bios.2011.10.054.

(20) Usachev, E. v.; Usacheva, O. v.; Agranovski, I. e. Surface Plasmon Resonance–Based Real-Time Bioaerosol Detection. *Journal of Applied Microbiology* **2013**, *115* (3), 766–773. https://doi.org/10.1111/jam.12267.

(21) Schwarzmeier, K.; Knauer, M.; Ivleva, N. P.; Niessner, R.; Haisch, C. Bioaerosol Analysis Based on a Label-Free Microarray Readout Method Using Surface-Enhanced Raman Scattering. *Anal Bioanal Chem* **2013**, *405* (16), 5387–5392. https://doi.org/10.1007/s00216-013-6984-0.

(22) Stanley, W. R.; Kaye, P. H.; Foot, V. E.; Barrington, S. J.; Gallagher, M.; Gabey, A. Continuous Bioaerosol Monitoring in a Tropical Environment Using a UV Fluorescence Particle Spectrometer. *Atmospheric Science Letters* **2011**, *12* (2), 195–199. https://doi.org/10.1002/asl.310.

(23) Ruske, S.; Topping, D. O.; Foot, V. E.; Kaye, P. H.; Stanley, W. R.; Crawford, I.; Morse, A. P.; Gallagher, M. W. Evaluation of Machine Learning Algorithms for Classification of Primary Biological Aerosol Using a New UV-LIF Spectrometer. *Atmospheric Measurement Techniques* **2017**, *10* (2), 695–708. https://doi.org/10.5194/amt-10-695-2017.

(24) Wu, Y.-C.; Shiledar, A.; Li, Y.-C.; Wong, J.; Feng, S.; Chen, X.; Chen, C.; Jin, K.; Janamian, S.; Yang,

Z.; Ballard, Z. S.; Göröcs, Z.; Feizi, A.; Ozcan, A. Air Quality Monitoring Using Mobile Microscopy and Machine Learning. *Light Sci Appl* **2017**, *6* (9), e17046–e17046. https://doi.org/10.1038/lsa.2017.46.

(25) Wu, Y.; Calis, A.; Luo, Y.; Chen, C.; Lutton, M.; Rivenson, Y.; Lin, X.; Koydemir, H. C.; Zhang, Y.; Wang, H.; Göröcs, Z.; Ozcan, A. Label-Free Bioaerosol Sensing Using Mobile Microscopy and Deep Learning. *ACS Photonics* **2018**, *5* (11), 4617–4627. https://doi.org/10.1021/acsphotonics.8b01109.

(26) Hinds, W. C. *Aerosol Technology: Properties, Behavior, and Measurement of Airborne Particles*; John Wiley & Sons, 2012.

(27) Dzubay, T. G.; Stevens, R. K. Ambient Air Analysis with Dichotomous Sampler and X-Ray Fluorescence Spectrometer. *Environ. Sci. Technol.* **1975**, *9* (7), 663–668. https://doi.org/10.1021/es60105a011.

(28) Sioutas, C.; Koutrakis, P.; Burton, R. Development of a Low Cutpoint Slit Virtual Impactor for Sampling Ambient Fine Particles. *Journal of Aerosol Science* **1994**, *25* (7), 1321–1330. https://doi.org/10.1016/0021-8502(94)90128-7.

(29) Drinovec, L.; Sciare, J.; Stavroulas, I.; Bezantakos, S.; Pikridas, M.; Unga, F.; Savvides, C.; Višić, B.; Remškar, M.; Močnik, G. A New Optical-Based Technique for Real-Time Measurements of Mineral Dust Concentration in PM_{10} Using a Virtual Impactor. *Atmospheric Measurement Techniques* **2020**, *13* (7), 3799–3813. https://doi.org/10.5194/amt-13-3799-2020.

(30) Kauppinen, E. I.; Jäppinen, A. V. K.; Hillamo, R. E.; Rantio-Lehtimäki, A. H.; Koivikko, A. S. A Static Particle Size Selective Bioaerosol Sampler for the Ambient Atmosphere. *Journal of Aerosol Science* **1989**, *20* (7), 829–838. https://doi.org/10.1016/0021-8502(89)90093-1.

(31) Paprotny, I.; Doering, F.; White, R. M. MEMS Particulate Matter (PM) Monitor for Cellular Deployment. In *2010 IEEE SENSORS*; 2010; pp 2435–2440. https://doi.org/10.1109/ICSENS.2010.5690758.

(32) Jianwen, S.; Kun, Y.; Zewen, L.; Yanwu, L. A System of Continuous Particles Monitoring Using Virtual Impactor. In *2015 12th IEEE International Conference on Electronic Measurement & Instruments (ICEMI)*; 2015; Vol. 03, pp 1183–1187. https://doi.org/10.1109/ICEMI.2015.7494466.

(33) Dong, M.; Iervolino, E.; Santagata, F.; Zhang, G.; Zhang, G. Integrated Virtual Impactor Enabled PM2.5 Sensor. *IEEE Sensors Journal* **2017**, *17* (9), 2814–2821. https://doi.org/10.1109/JSEN.2017.2683443.

(34) Wang, Y.; Wang, Y.; Chen, D.; Liu, X.; Wu, C.; Xie, J. A Miniature System for Separation and Detection of PM Based on 3-D Printed Virtual Impactor and QCM Sensor. *IEEE Sensors Journal* **2018**, *18* (15), 6130–6137. https://doi.org/10.1109/JSEN.2018.2844876.

(35) Wang, Y.; Wang, Y.; Liu, W.; Chen, D.; Wu, C.; Xie, J. An Aerosol Sensor for PM1 Concentration Detection Based on 3D Printed Virtual Impactor and SAW Sensor. *Sensors and Actuators A: Physical* **2019**, *288*, 67–74. https://doi.org/10.1016/j.sna.2019.01.013.

(36) Park, D.; Kim, Y.-H.; Woo Park, C.; Hwang, J.; Kim, Y.-J. New Bio-Aerosol Collector Using a Micromachined Virtual Impactor. *Journal of Aerosol Science* **2009**, *40* (5), 415–422. https://doi.org/10.1016/j.jaerosci.2008.12.007.

(37) Nasrabadi, A. M.; Park, J.-W.; Kim, H. S.; Han, J. S.; Hyun, J.; Yong, D.; Hwang, J. Assessment of Indoor Bioaerosols Using a Lab-Made Virtual Impactor. *Aerosol Science and Technology* **2017**, *51* (2), 159–167. https://doi.org/10.1080/02786826.2016.1246707.

(38) Bergman, W.; Lochner, J. S., R.; Sawyer, S.; Milanovich, F.; Mariella Jr., R. High Air Flow, Low Pressure Drop, Bio-Aerosol Collector Using a Multi-Slit Virtual Impactor. *Journal of Aerosol Science* **2005**, *36* (5), 619–638. https://doi.org/10.1016/j.jaerosci.2004.12.010.

(39) Xu, Z.; Wu, Y.; Shen, F.; Chen, Q.; Tan, M.; Yao, M. Bioaerosol Science, Technology, and Engineering: Past, Present, and Future. *Aerosol Science and Technology* **2011**, *45* (11), 1337–1349. https://doi.org/10.1080/02786826.2011.593591.

(40) Lo, F.; Bitz, C. M.; Battisti, D. S.; Hess, J. J. Pollen Calendars and Maps of Allergenic Pollen in North America. *Aerobiologia* **2019**, *35* (4), 613–633.

(41) Jeong, K. Y.; Son, M.; Park, J. H.; Park, K. H.; Park, H. J.; Lee, J.-H.; Hong, C.-S.; Park, J.-W. Cross-Reactivity between Oak and Birch Pollens in Korean Tree Pollinosis. *Journal of Korean medical science* **2016**, *31* (8), 1202–1207.

(42) Kim, Y.; Oh, I.; Lee, J.; Sim, C. S.; Oh, Y. S.; Lee, J.-H. Astigmatism Associated with Allergic Conjunctivitis in Urban School Children. *Journal of Ophthalmology* **2019**, *2019*.

(43) Ross, A. M.; Corden, J. M.; Fleming, D. M. The Role of Oak Pollen in Hay Fever Consultations in General Practice and the Factors Influencing Patients' Decisions to Consult. *British Journal of General Practice* **1996**, *46* (409), 451–455.

(44) Calabria, C. W.; Dice, J. P.; Hagan, L. L. Prevalence of Positive Skin Test Responses to 53 Allergens in Patients with Rhinitis Symptoms. In *Allergy and asthma proceedings*; OceanSide Publications, 2007; Vol. 28, p 442.

(45) Dales, R. E.; Cakmak, S.; Judek, S.; Coates, F. Tree Pollen and Hospitalization for Asthma in Urban Canada. *International archives of allergy and immunology* **2008**, *146* (3), 241–247.

(46) Seo, S.; Su, T.-W.; Tseng, D. K.; Erlinger, A.; Ozcan, A. Lensfree Holographic Imaging for On-Chip Cytometry and Diagnostics. *Lab Chip* **2009**, *9* (6), 777–787. https://doi.org/10.1039/B813943A.

(47) Tseng, D.; Mudanyali, O.; Oztoprak, C.; Isikman, S. O.; Sencan, I.; Yaglidere, O.; Ozcan, A. Lensfree Microscopy on a Cellphone. *Lab Chip* **2010**, *10* (14), 1787–1792. https://doi.org/10.1039/C003477K.

(48) Bishara, W.; Su, T.-W.; Coskun, A. F.; Ozcan, A. Lensfree On-Chip Microscopy over a Wide Field-of-View Using Pixel Super-Resolution. *Opt. Express, OE* **2010**, *18* (11), 11181–11191. https://doi.org/10.1364/OE.18.011181.

(49) Mudanyali, O.; Tseng, D.; Oh, C.; Isikman, S. O.; Sencan, I.; Bishara, W.; Oztoprak, C.; Seo, S.; Khademhosseini, B.; Ozcan, A. Compact, Light-Weight and Cost-Effective Microscope Based on Lensless Incoherent Holography for Telemedicine Applications. *Lab Chip* **2010**, *10* (11), 1417–1428. https://doi.org/10.1039/C000453G.

(50) Greenbaum, A.; Luo, W.; Su, T.-W.; Göröcs, Z.; Xue, L.; Isikman, S. O.; Coskun, A. F.; Mudanyali, O.; Ozcan, A. Imaging without Lenses: Achievements and Remaining Challenges of Wide-Field on-Chip Microscopy. *Nature Methods* **2012**, *9* (9), 889–895. https://doi.org/10.1038/nmeth.2114.

(51) Su, T.-W.; Xue, L.; Ozcan, A. High-Throughput Lensfree 3D Tracking of Human Sperms Reveals Rare Statistics of Helical Trajectories. *Proceedings of the National Academy of Sciences* **2012**, *109* (40), 16018–16022. https://doi.org/10.1073/pnas.1212506109.

(52) Daloglu, M. U.; Lin, F.; Chong, B.; Chien, D.; Veli, M.; Luo, W.; Ozcan, A. 3D Imaging of Sex-Sorted Bovine Spermatozoon Locomotion, Head Spin and Flagellum Beating. *Sci Rep* **2018**, *8* (1), 15650. https://doi.org/10.1038/s41598-018-34040-3.

(53) Esch, R.; Hartsell, C.; Crenshaw, R.; Jacobson, R. Common Allergenic Pollens, Fungi, Animals, and Arthropods. *Clinical reviews in allergy & immunology* **2001**, *21*, 261–292. https://doi.org/10.1385/CRIAI:21:2-3:261.

(54) D'Amato, G.; Spieksma, F. Th. M.; Liccardi, G.; Jäger, S.; Russo, M.; Kontou-Fili, K.; Nikkels, H.; Wüthrich, B.; Bonini, S. Pollen-Related Allergy in Europe*. *Allergy* **1998**, *53* (6), 567–578. https://doi.org/10.1111/j.1398-9995.1998.tb03932.x.

(55) Zhang, Y.; Wang, H.; Wu, Y.; Tamamitsu, M.; Ozcan, A. Edge Sparsity Criterion for Robust Holographic Autofocusing. *Opt. Lett., OL* **2017**, *42* (19), 3824–3827. https://doi.org/10.1364/OL.42.003824.

(56) Huang, G.; Liu, Z.; van der Maaten, L.; Weinberger, K. Q. Densely Connected Convolutional Networks. arXiv January 28, 2018.

(57) Gastaminza, G.; Lombardero, M.; Bernaola, G.; Antepara, I.; Munoz, D.; Gamboa, P. M.; Audicana, M. T.; Marcos, C.; Ansotegui, I. J. Allergenicity and Cross-Reactivity of Pine Pollen. *Clinical & Experimental Allergy* **2009**, *39* (9), 1438–1446.

(58) Rivenson, Y.; Zhang, Y.; Günaydın, H.; Teng, D.; Ozcan, A. Phase Recovery and Holographic Image Reconstruction Using Deep Learning in Neural Networks. *Light: Science &Amp; Applications* **2018**, *7*, 17141.

(59) Barbastathis, G.; Ozcan, A.; Situ, G. On the Use of Deep Learning for Computational Imaging. *Optica, OPTICA* **2019**, *6* (8), 921–943. https://doi.org/10.1364/OPTICA.6.000921.

(60) Wu, Y.; Rivenson, Y.; Zhang, Y.; Wei, Z.; Günaydin, H.; Lin, X.; Ozcan, A. Extended Depth-of-Field in Holographic Imaging Using Deep-Learning-Based Autofocusing and Phase Recovery. *Optica* **2018**, *5* (6), 704. https://doi.org/10.1364/OPTICA.5.000704.

(61) Rivenson, Y.; Wu, Y.; Ozcan, A. Deep Learning in Holography and Coherent Imaging. *Light Sci Appl* **2019**, *8* (1), 1–8. https://doi.org/10.1038/s41377-019-0196-0.

(62) Göröcs, Z.; Tamamitsu, M.; Bianco, V.; Wolf, P.; Roy, S.; Shindo, K.; Yanny, K.; Wu, Y.; Koydemir, H. C.; Rivenson, Y.; Ozcan, A. A Deep Learning-Enabled Portable Imaging Flow Cytometer for Cost-Effective, High-Throughput, and Label-Free Analysis of Natural Water Samples. *Light: Science & Applications* **2018**, *7* (1), 66. https://doi.org/10.1038/s41377-018-0067-0.

(63) Göröcs, Z.; Baum, D.; Song, F.; Haan, K. de; Koydemir, H. C.; Qiu, Y.; Cai, Z.; Skandakumar, T.; Peterman, S.; Tamamitsu, M.; Ozcan, A. Label-Free Detection of Giardia Lamblia Cysts Using a Deep Learning-Enabled Portable Imaging Flow Cytometer. *Lab Chip* **2020**, *20* (23), 4404–4412. https://doi.org/10.1039/D0LC00708K.

(64) Mittal, S. A Survey on Optimized Implementation of Deep Learning Models on the NVIDIA Jetson Platform. *Journal of Systems Architecture* **2019**, *97*, 428–442.

(65) Mirzaee, I.; Song, M.; Charmchi, M.; Sun, H. A Microfluidics-Based on-Chip Impinger for Airborne Particle Collection. *Lab on a Chip* **2016**, *16* (12), 2254–2264.

(66) Bhardwaj, P.; Bagdi, P.; Sen, A. K. Microfluidic Device Based on a Micro-Hydrocyclone for Particle–Liquid Separation. *Lab on a Chip* **2011**, *11* (23), 4012–4021.

(67) Liang, W.; Austin, R. H.; Sturm, J. C. Scaling of Deterministic Lateral Displacement Devices to a Single Column of Bumping Obstacles. *Lab on a Chip* **2020**, *20* (18), 3461–3467.

(68) Dhar, M.; Lam, J. N.; Walser, T.; Dubinett, S. M.; Rettig, M. B.; Di Carlo, D. Functional Profiling of Circulating Tumor Cells with an Integrated Vortex Capture and Single-Cell Protease Activity Assay. *Proceedings of the National Academy of Sciences* **2018**, *115* (40), 9986–9991.

Figures

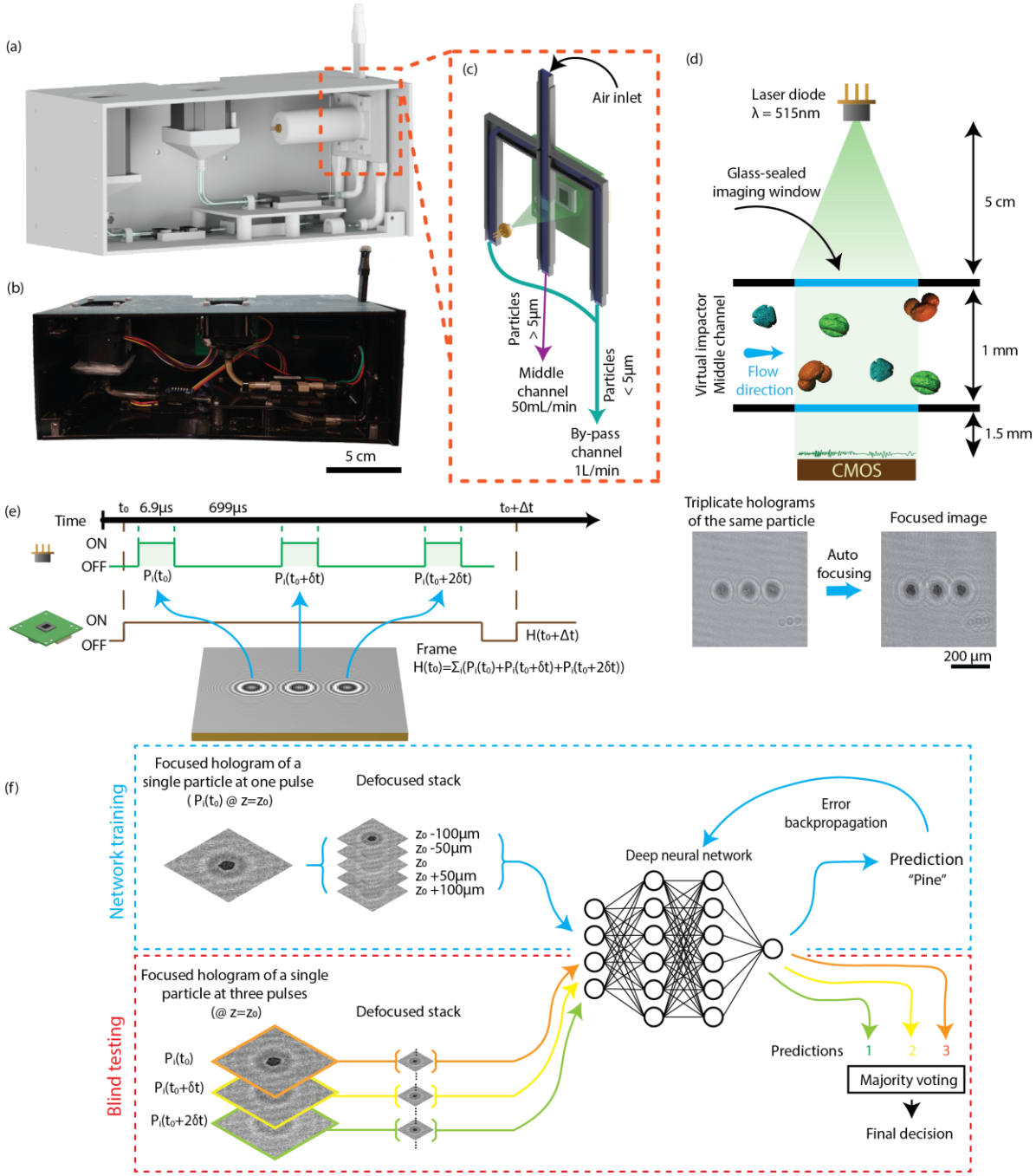

Figure 1. The virtual impactor-based label-free pollen detection device. (a) 3D computer-aided-design (CAD) drawing of the device. (b) Photograph of the prototype. Major parts of the device were 3D printed. (c) Schematic drawing of the virtual impactor channel used to concentrate the flowing aerosols and the lens-free imaging set-up. (d) Schematic drawing of the lens-free imaging system. A laser diode illuminated the particles flying through the imaging window with pulsed illumination. (e) Three pulses formed a pulse train. Particles cast lens-free inline holograms on a CMOS image sensor with each pulse. Triplicate holographic patterns are digitally integrated by the CMOS sensor on each frame. (f) A deep neural network was trained to classify pollen species. FOVs containing individual pollen particles were first auto-focused. The focused hologram was

intentionally defocused for ±50 and ±100μm in the axial direction. Both the real and imaginary channels of the focused and defocused holograms formed an image stack to train the network. In the blind testing stage, a majority voting was applied to the labels inferred using the triplicate holographic patterns of each flowing particle.

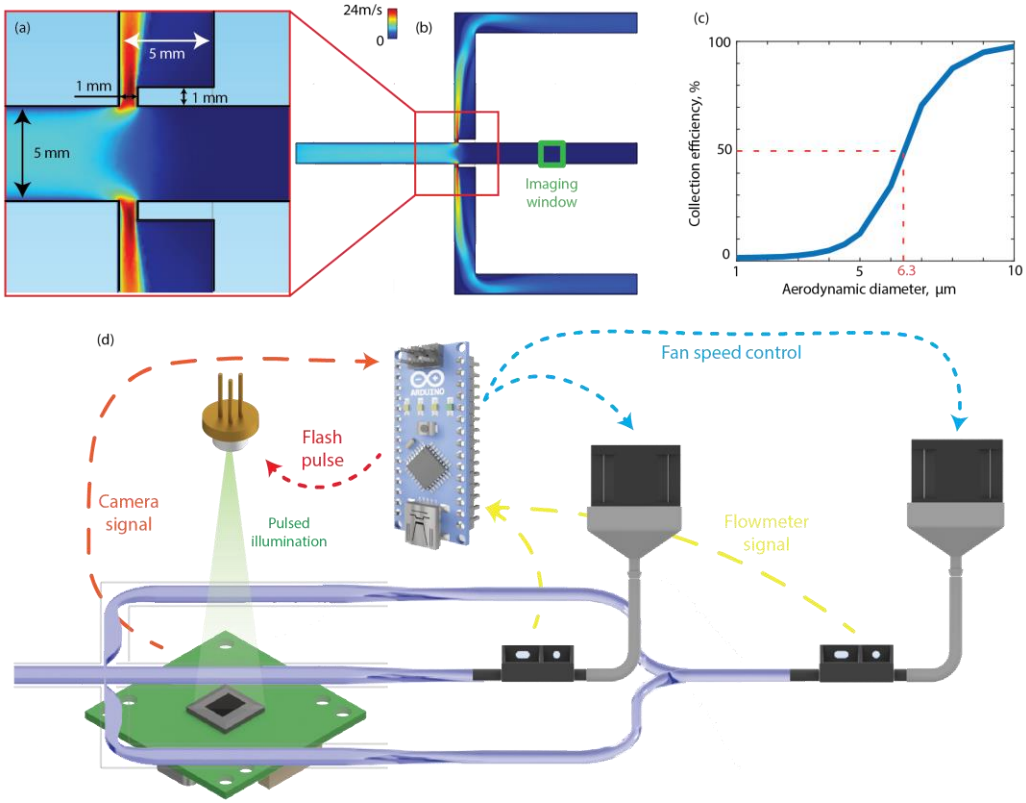

Figure 2. Design of the virtual impactor-based system. The geometrical design of the virtual impactor used to concentrate flowing particles was optimized using FEM simulations. (a-b) The flow field inside the channel. (c) Simulated particle collection efficiency in the middle channel of the virtual impactor. (d) Schematic drawing of the controlling circuit for the portable device. On the left, the circuit receives the signal from the CMOS image sensor and fires a pulse train. On the right, the circuit measures the flow rate inside the virtual impactor channel and uses it to adjust the fan power using a PID controller.

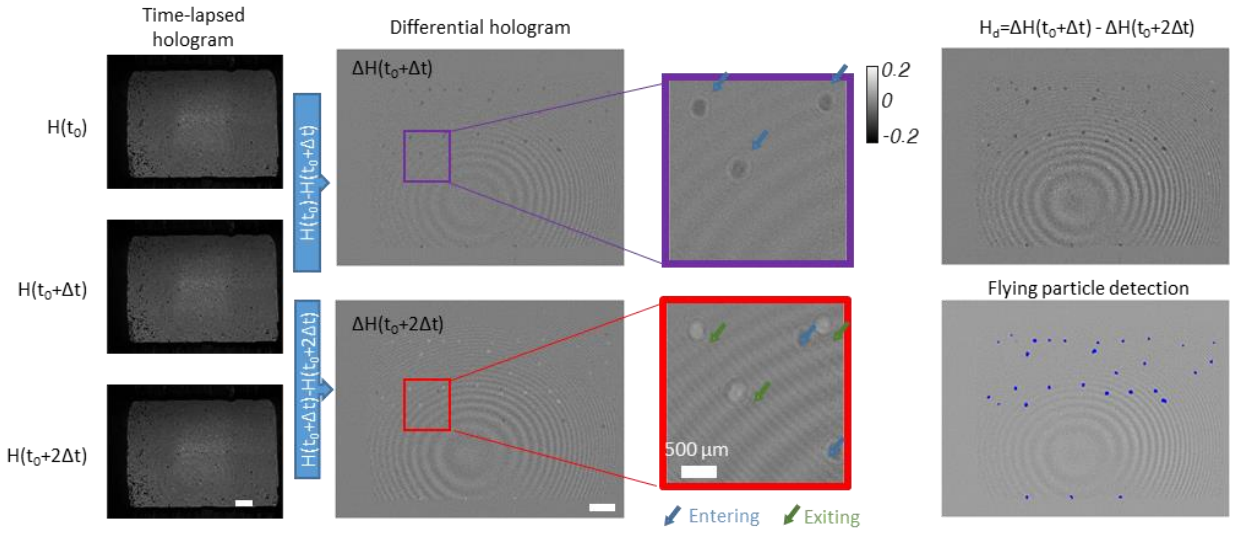

Figure 3. Flowing particle detection and localization using differential holograms. Differential holograms (see Eq. 1) were calculated using three successive holograms $H(t_0)$, $H(t_0 + \Delta t)$ and $H(t_0 + 2\Delta t)$. Note that Δt=285.7 ms and should not be confused with $\delta t = 699\mu s$ which is the interval between two successive pulses. One of these holographic images contains the entire triplicate hologram set of a flowing particle within the imaging window. Flying particles present lower intensity levels in the differential hologram H_d and a threshold was used to localize the flowing particles.

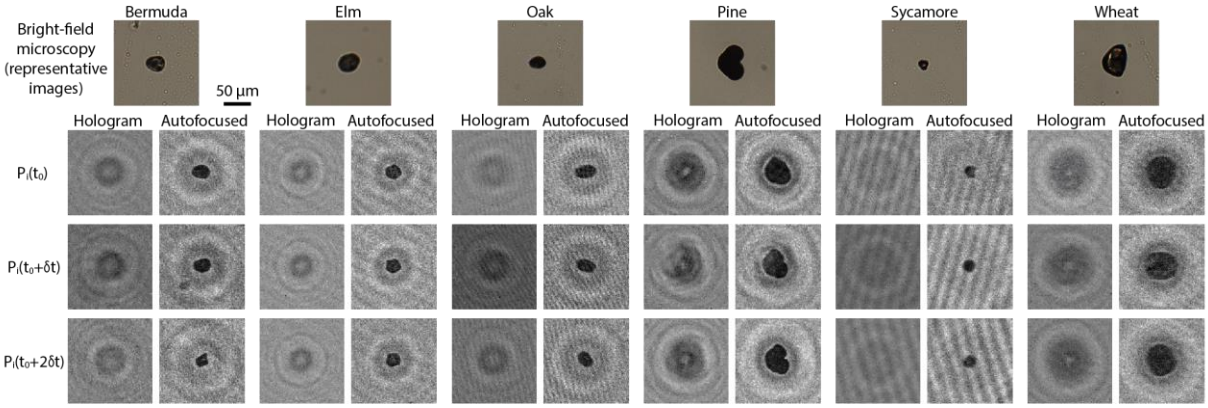

Figure 4. Triplicate holographic patterns of the same flowing particles under pulsed illumination; each pulse duration is 6.9 μs and $\delta t = 699\mu s$. Top row: a representative pollen particle of each species imaged under a bright-field microscope. Bottom three rows: triplicate holographic patterns of a different pollen particle of each species captured during our experiments; their autofocused images are also shown to the right of the corresponding lensfree hologram.

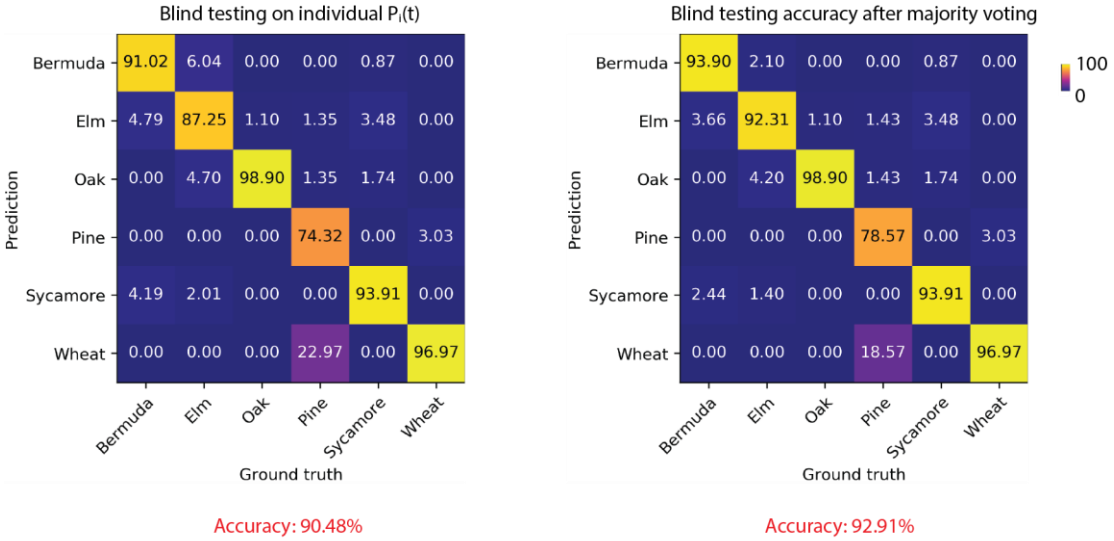

Figure 5. Confusion matrices of the classification deep neural network. (Left) In the blind testing stage, each image FOV is separately/individually classified, ignoring triplicate holograms of each flowing particle. (Right) A majority voting was applied to the three labels predicted by using the triplicate holographic patterns of each flowing particle. The final classification accuracy with majority voting improved to 92.91%.

TOC Graphic

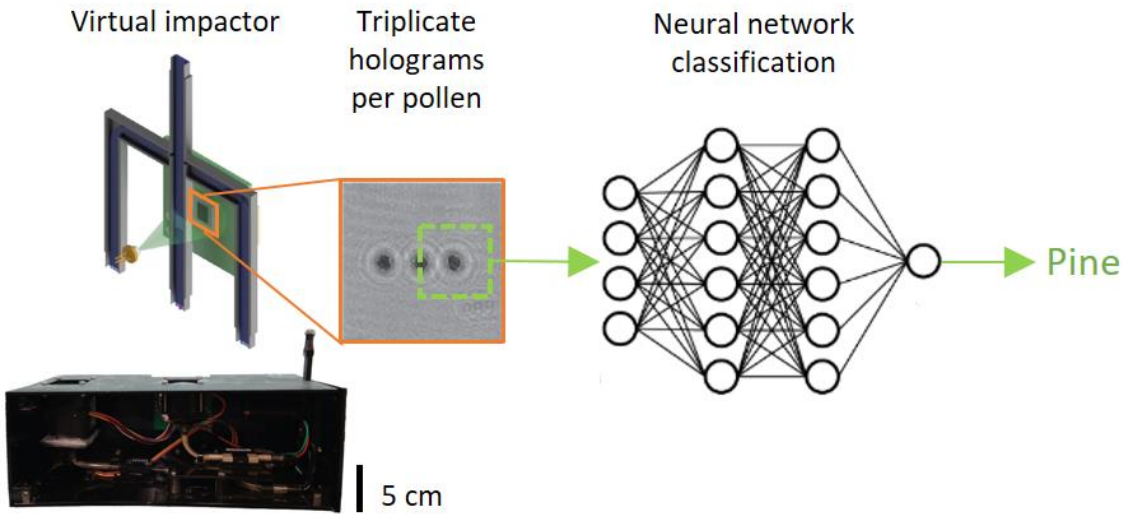
Virtual impactor
Triplicate holograms per pollen
Neural network classification
Pine
5 cm